ACS APPLIED MATERIALS & INTERFACES

www.acsami.org

Research Article

3D Bioprinted Tumor-Stroma Models of Triple-Negative Breast Cancer Stem Cells for Preclinical Targeted Therapy Evaluation

Patricia González-Callejo, Clara García-Astrain, Ada Herrero-Ruiz, Malou Henriksen-Lacey, Joaquín Seras-Franzoso, Ibane Abasolo, and Luis M. Liz-Marzán*

Cite This: *ACS Appl. Mater. Interfaces* 2024, 16, 27151−27163

Read Online

ACCESS | Metrics & More | Article Recommendations | Supporting Information

ABSTRACT: Breast cancer stem cells (CSCs) play a pivotal role in therapy resistance and tumor relapse, emphasizing the need for reliable *in vitro* models that recapitulate the complexity of the CSC tumor microenvironment to accelerate drug discovery. We present a bioprinted breast CSC tumor-stroma model incorporating triple-negative breast CSCs (TNB-CSCs) and stromal cells (human breast fibroblasts), within a breast-derived decellularized extracellular matrix bioink. Comparison of molecular signatures in this model with different clinical subtypes of bioprinted tumor-stroma models unveils a unique molecular profile for artificial CSC tumor models. We additionally demonstrate that the model can recapitulate the invasive potential of TNB-CSC. Surface-enhanced Raman scattering imaging allowed us to monitor the invasive potential of tumor cells in deep *z*-axis planes, thereby overcoming the depth-imaging limitations of confocal fluorescence microscopy. As a proof-of-concept application, we conducted high-throughput drug testing analysis to assess the efficacy of CSC-targeted therapy in combination with conventional chemotherapeutic compounds. The results highlight the usefulness of tumor-stroma models as a promising drug-screening platform, providing insights into therapeutic efficacy against CSC populations resistant to conventional therapies.

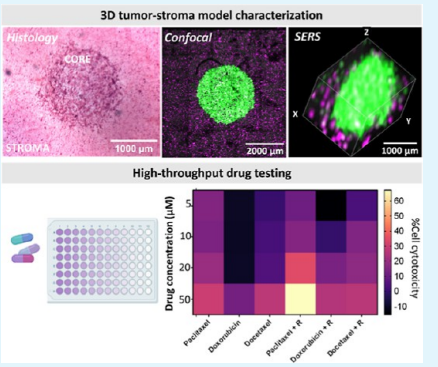

KEYWORDS: *triple-negative breast cancer, cancer stem cells, 3D bioprinting, tumor microenvironment, SERS*

1. INTRODUCTION

Breast cancer remains a global health challenge impacting millions of lives annually.[1] Despite significant improvements in our understanding of the disease, its clinical heterogeneity continues to hinder progress in developing effective therapies.[2] Among the various breast cancer subtypes, triple-negative breast cancer (TNBC) stands out for its high aggressiveness, attributed to the absence of hormone receptor (HR) expression, basal-like cell characteristics, and genetic variability. These factors add complexity to the development of specific interventions for this subtype of breast cancer.[3]

Indeed, therapy resistance poses a significant difficulty for TNBC patients.[4] While initially responsive to treatment, prolonged administration often leads to resistance development, ultimately resulting in a poor prognosis.[5] This resistance is primarily orchestrated by breast cancer stem cells (CSCs), which have the unique capacity for self-renewal and multilineage progenitor expansion.[6,7] Breast CSCs constitute a subset of cancer cells with the ability to initiate tumorigenesis, metastasis, and resistance to treatment.[8,9] Consequently, it is imperative to prioritize the development of targeted therapies against CSC to mitigate the risk of recurrence and metastasis following therapy.[10,11] In this context, the development of effective preclinical tumor models, capable of replicating the biological nature of real tumors, will help accelerate drug discovery in this area, thereby allowing the exploration of new targeted approaches against this cell population.[12,13]

Although traditional preclinical *in vitro* two-dimensional (2D) cell culture models have been most valuable in cancer research, they often fall short in replicating tumor complexity.[14] Breast tumors typically exhibit a spatial arrangement characterized by clusters of tumor cells enveloped by the surrounding connective tissue, known as stroma.[15] The stroma plays a pivotal role in tumor development and therapeutic response, through specialized cells within the tumor microenvironment (TME). The TME is characterized by a complex bidirectional communication network involving cancer cells, stromal cells, and extracellular matrix (ECM) components.[16−18] Replicating such interactions in an artificial *in vitro* setting remains challenging, mainly due to difficulties in achieving the correct spatial deposition of specific cell populations.[19] Three-dimensional (3D) bioprinting therefore emerges as a promising technology to address the challenge of

Received: March 13, 2024
Revised: May 8, 2024
Accepted: May 8, 2024
Published: May 20, 2024

mimicking the breast TME.[20−22] With precise 3D construction in a reproducible and automated manner, bioprinting offers the possibility to construct 3D platforms with a controlled integration of various cell types and ECM components, closely mimicking the heterogeneous and dynamic nature of the breast TME.[20,23,24] Bioprinted tumor models provide a more representative *in vitro* tumor environment for evaluating therapeutic efficacy and toxicity of anticancer drugs.[25,26]

The use of decellularized extracellular matrices (dECMs) as bioinks presents significant advantages in 3D bioprinting because they offer enhanced biological relevance and physiological mimicry, when compared to traditional bioinks.[27−31] dECM bioinks, which are obtained by removing cellular and genetic components from tissue sources, provide a more authentic representation of the native tissue environment, thereby fostering improved cell−matrix interactions.[29−31] However, the inherent complexity of dECM viscosity hinders bioprinting of well-defined structures with high precision.[32] To overcome this challenge, researchers often combine dECM-based bioinks with other biopolymers such as gelatin, hyaluronic acid, or their methacrylated counterparts for improved cross-linking to ensure the necessary consistency for accurate 3D printing.[32−34] However, addition of exogenous components alters the natural composition of the original dECM (particularly in terms of mechanical properties and ECM composition), thereby complicating recreation of the original tissue microenvironment.

Monitoring cell behavior in 3D models poses another significant challenge, particularly when aiming at prolonged observation times. One of the main difficulties involves the limited penetration depth of light into the models, which hinders effective 3D imaging. Confocal fluorescence microscopy (CFM) stands as the gold standard for cell imaging with exceptional resolution along the *xyz*-axes.[35] However, CFM also faces certain drawbacks, particularly when applied to extended studies. Challenges include photobleaching and the limited penetration of excitation laser and emitted light through relatively thick 3D cellular systems, among others. Alternatively, surface-enhanced Raman spectroscopy (SERS) has emerged as a versatile tool for monitoring 3D cell models with high resolution, especially in the *z* direction.[35] This innovative technique employs SERS-labeled plasmonic nanoparticles (NPs), known as SERS tags, which consist of gold NPs covered by a monolayer of Raman-active molecules (Raman reporters, RaRs), which are subsequently protected by an external polymeric coating.[36] SERS tags can efficiently label diverse cell populations, offering noncytotoxic cell multiplexing. The use of SERS (as opposed to CFM) yields several advantages, including the use of a single laser source to irradiate different SERS tags—and thus cell populations—, absence of photobleaching, and responsiveness in the near-infrared, which facilitates deeper penetration into biological systems with minimum photocytotoxicity. The combination of SERS with CFM offers new possibilities for the biocompatible high-resolution monitoring of 3D cell models with increased depth and over long time periods.[36]

We introduce herein an approach toward the development of 3D bioprinted TNBC−CSC tumor-stroma models by directly bioprinting the tumor core within a supportive bath of breast dECM containing stromal cells. In contrast to other works that focus on either the use of preformed spheroids embedded in ECM matrices or microfluidic devices to control the distribution of different cell populations, this strategy allows us to obtain reproducible structures in an automated fashion. The 3D models accurately replicate the arrangement and architecture of breast carcinoma while preserving the ECM composition, thus allowing cell-ECM communication *in situ*. Indeed, whereas previous studies have primarily concentrated on constructing 3D models of bulk tumor cells, our TNBC−CSC tumor stroma models provide a promising platform for examining the behavior of CSC populations, known for their distinctive protumoral functions, within a sophisticated 3D environment. These TNBC−CSC tumor-stroma models display a unique molecular signature associated with the CSC TME. We additionally demonstrate the compatibility of dECM-based inks with SERS tags for 3D imaging of breast cancer models. The use of bioprinting technology to fabricate CSC tumor-stroma 3D models enables high-throughput platforms for preclinical screening, which will facilitate the evaluation of therapeutic compound combinations, ultimately aiding in the selection of the most effective drug candidates for targeting and eliminating specific CSC populations.

2. EXPERIMENTAL SECTION

2.1. Materials. Hexadecyltrimethylammonium bromide (CTAB, ≥99.0%), hydrogen tetrachloroaurate trihydrate ($HAuCl_4 \cdot 3H_2O$, ≥99.9%), silver nitrate ($AgNO_3$, ≥99.9%), L-ascorbic acid (ascorbic acid (AA), ≥99%), sodium borohydride ($NaBH_4$, 99%), *O*-[2-(3-mercaptopropionylamino)ethyl]-*O*′-methylpolyethylene glycol (PEG, MW 5000 g/mol), biphenyl-4-thiol (4BPT, 97%), 2-naphthalenethiol (2NAT, 99%), poly(isobutylene-*alt*-maleic anhydride) (average MW ∼ 6000 g/mol), poly-L-arginine hydrochloride (PA, Aldrich no. 26982−20−7 > 70 000 Da), dodecylamine (98%), tetrahydrofuran (99.85%, extra dry), chloroform ($CHCl_3$, ≥99.8%), sodium hydroxide (NaOH, >97%), and oleylamine (OAm, 70%) were all purchased from Sigma-Aldrich. The amphiphilic polymer dodecylamine-grafted (75%) poly(isobutylene-*alt*-maleic anhydride) was synthesized following published procedures.[37,38] All chemicals were used as received. Milli-Q water was used in all experiments. All pieces of glassware used for NP synthesis were washed with aqua regia, rinsed with water, and dried before use.

2.2. NP Synthesis. The synthesis of the NPs employed in this study was conducted following a seed-mediated millifluidic reactor protocol.[39] In the synthesis of Au nanorods (AuNRs), seed preparation involved the rapid reduction of a 20 mL $HAuCl_4$ 1 mM solution in 100 mM CTAB using a 2.4 mL $NaBH_4$ 12 mM aqueous solution. This process employed two of the pumps within the flow reactor, maintaining a total flow rate of 11.2 mL/min. The solution was kept for 30 min at room temperature to remove excess borohydride. The synthesis of AuNRs in the flow reactor was performed by using three pumps at various phases of the process. To initiate AuNR growth, a solution comprising 50 mL of 100 mM CTAB containing 1 mM $HAuCl_4$ and 0.24 mM $AgNO_3$ under acidic conditions (pH 3−4) was mixed with a solution of 25 mL of 3.2 mM AA in 100 mM CTAB. After the prereduction of Au(III) to Au(I) in the mixing tube, 25 mL of 100 mM CTAB containing 800 μL of seeds was introduced, with a total flow rate of 20 mL/min. The mixture was then left undisturbed for 4 h. The resulting colloidal dispersion was centrifuged at 8000 rpm for 20 min, the precipitate was collected, and AuNRs (longitudinal localized surface plasmon band at 780 nm) were redispersed in a 1 mM CTAB solution.

Au nanostars (AuNSs) were prepared in the same millifluidic flow reactor using seeds prepared in batch. Gold seeds were synthesized by the addition of 4.2 mL of sodium citrate 0.1 M to 250 mL of boiling $HAuCl_4$ 0.5 mM solution under vigorous stirring. After 15 min, the solution was cooled down and stored at 4 °C until further use. AuNS synthesis involved directly mixing the three precursor solutions through the pumps of the flow reactor. In this process, we simultaneously combined a 20 mL of aqueous solution containing $HAuCl_4$ 1 mM, HCl 3.82 mM, and 760 μL of seeds while

https://doi.org/10.1021/acsami.4c04135
ACS Appl. Mater. Interfaces 2024, 16, 27151−27163

concurrently introducing 10 mL of AA 3.82 mM and 10 mL of $AgNO_3$ 0.23 mM, maintaining a total flow rate of 10 mL/min. To the resulting AuNS dispersion, 50 μL of PEG 1 mM was added, and the solution was stirred for 15 min. Finally, the AuNS dispersion was centrifuged at 2000 rpm for 10 min and the precipitate was redispersed in water.

2.3. SERS Tags. AuNSs coated with 2NAT and AuNRs coated with 4BPT were synthesized and characterized as previously reported.[35] The final concentration of the SERS tags was [Au^0] = 0.5 mM, corresponding to 1.9×10^{10} NP/mL. We employed 4BPT-coated AuNRs (AuNR@4BPT) to label MCF-7, MDA-MB-231, and CSC cells, whereas human breast fibroblast (HBF) cells were labeled with 2NAT-coded AuNSs (AuNS@2NAT). SERS tags were coated with (positively charged) poly-L-arginine hydrochloride (PA) to enhance cell uptake, as previously reported.[40]

2.4. ECM Decellularization and Bioink Formulation. Porcine breast tissue was obtained from the slaughterhouse and stored at −80 °C until needed. Breast tissue was used for the dECM bioink formulation at a final concentration of 20 mg/mL (2% w/v), as previously described.[34]

2.5. Cell Culture. Primary HBFs were purchased from Innoprot (Derio, Spain), and human breast MDA-MB-231, MCF-7, and THP-1 cell lines were obtained from American Type Culture Collection. MDA-MB-231 ALDH/tdTomato CSCs were generated as previously described.[41−44] Briefly, this process involved the stable transfection of MDA-MB-231 cells with a vector expressing the tdTomato fluorescent protein under the regulatory control of the ALDH1A1 promoter specific to CSC, facilitating fluorescent labeling and isolation of CSCs expressing ALDH1A1. CSC subpopulations from MDA-MB-231 ALDH/tdTomato were isolated according to their tdTomato expression in a fluorescent-activated cell sorter Aria cell sorter (BD Biosciences, Franklin Lakes, NJ).[41−44] All cell lines were cultured in Dulbecco's modified Eagle's medium (DMEM) supplemented with 10% fetal bovine serum and 1% penicillin/streptomycin (Fisher Scientific) and cultured under standard tissue culture conditions at 37 °C with 5% CO_2.

2.6. Biocompatibility of dECM Gels. To assess cell viability within the dECM bioink, cells were mixed with the dECM bioink at a concentration of 5×10^5 cells/mL, seeded in Ibidi eight-well plates, and maintained in culture for 5 days. Cell viability was monitored using a live/dead cell assay by incubating 3D cell cultures with Calcein AM (1/100) and PI (1/50), for 20 min. The corresponding confocal images were processed using ImageJ software.

2.7. Bioprinting of Tumor-Stroma Model. The tumor compartment of the constructs comprised MCF-7, MDA-MB-231, or MDA-MB-231 isolated CSCs. The stromal compartment comprised 100% HBFs or 50% HBFs and 50% THP-1 cells (cell number ratio), depending on the assay to be performed. Prior to bioprinting, cells were fluorescently labeled with different fluorescent cell trackers. Cancer cells were stained with CellTracker Green CMFDA Dye, HBFs with CellTracker Deep Red, and THP-1 cells with CellTracker Blue CMF_2HC Dye (all from ThermoFisher). For the stromal compartment bioink formulation, either HBF or HBF and THP-1 cells were mixed in the appropriate proportions inside the dECM bioink at a concentration of 1×10^7 total cells/mL. For the tumor compartment, cancer cells were mixed in the dECM bioink at 2×10^7 cells/mL and bioprinted (RegenHU Discovery bioprinter, Switzerland) in the center of the 1 cm^2 well of an Ibidi eight-well chamber slide (Ibidi) containing the stromal cell bioink 50 μL, previously pipetted into the well plates. Tumor cores were printed as four-layered circular structures with a printing design of 1 mm in diameter. dECM bioinks were extruded through a dispensing needle with an internal diameter of 0.3 mm (Nordson) at 10 °C, a pressures of 0.18−0.20 MPa, and printing speeds of 0.5−1 mm/s. Immediately following bioprinting, tumor-stroma models were placed at 37 °C to promote dECM bioink cross-linking. Tumor-stroma constructs measured 1 cm × 1 cm × 3 mm (length, width, and height). After 20 min, complete DMEM (300 μL) was added to the chamber slide. Constructs were then incubated for up to 14 days.

2.8. Tumor-Stroma 3D Model Confocal Imaging. All confocal images were recorded in a Zeiss LSM 880 confocal laser scanning microscope, equipped with 405 nm (blue fluorophore excitation), 488 nm (green fluorophore excitation), and 633 nm (far red fluorophore excitation) lasers and Plan-Apochromat 10 × (0.45 NA) and Plan-Apochromat 20× (0.8 NA) objectives. For 3D characterization of tumor models, *z*-stacks (ca. 50 μm thick) were obtained, and a postimaging maximum intensity projection (MIP) filter and 3D render series filters were applied.

2.9. Histological Analysis of the Tumor-Stroma Model. For histological analysis, tissues were fixed in 4% paraformaldehyde (Electron Microscopy Sciences, Hatfield, PA) for 20 min at 37 °C and left overnight in 30% (w/v) sucrose solution at 4 °C, prior to embedding them in OCT tissue freezing medium. Frozen blocks were stored at −80 °C until needed. Tissue sections (7 μm) were stained with Hematoxylin and Eosin (H&E) and Picrosirius red.

2.10. Immunofluorescence Assays. For immunofluorescence (IF) images, 3D tumor-stroma models were washed twice with phosphate-buffered saline (PBS), fixed with paraformaldehyde 4% (20 min, RT), and left overnight in a 30% (w/v) sucrose solution at 4 °C, prior to embedding them in OCT tissue freezing medium. Frozen blocks were stored at −80 °C until needed. Tissue cryosections (30 μm) were then permeabilized with 0.5% Triton X-100 (20 min, RT) and blocked with 2% bovine serum albumin + 0.1% Triton X-100 in PBS overnight, followed by overnight incubation with primary antibodies (1:200, 4 °C), washed and incubated with secondary antibodies for 1 h, (1:1000, 4 °C) and with DAPI (20 min, RT). The list of antibodies is detailed in Table S1 (Supporting Information). IF images were acquired on a Zeiss LSM 880 confocal microscope with Zen software (Zeiss Microscopy), and image analysis was performed using ImageJ and Graphpad software.

2.11. Oncoproteome Profiling. Proteome Profiler Human XL Oncology Array assays (R&D Systems, ARY026) were performed according to the manufacturer's protocol. In brief, cell lysates from two biological replicates of 3D models comprising stroma and MCF-7, MDA-MB-231, and CSC tumor-stroma models were collected and added to the array membranes and then incubated overnight at 4 °C. Membranes were washed, incubated with a streptavidin-HRP-coupled antibody (1:2000) for 30 min at RT, and developed using Chemi-Reagent Mix. Images were captured and visualized using the LI-COR Odyssey Fc imaging system, and dot-integrated densities were measured using ImageJ. Integrated density was calculated as the product of the area of a selected region of interest (ROI) and its mean pixel intensity. ROI areas were manually selected by drawing a region around each dot of the membrane. Dot-integrated density values for each sample were normalized to control dot-integrated density for each membrane.

2.12. Spheroid 3D Invasion Assay. HBF and cancer cells (MDA-MB-231, MCF-7, and CSC) were labeled with cell trackers and seeded at a 1:1 ratio (2×10^4 cells/spheroid) in ultralow attachment spheroid plates (Thermo 96U Bottom plate). After 24 h in culture, spheroids were collected from the plate and deposited in Ibidi 96 well imaging plates containing dECM (250 μL). 3D invasion within the dECM was then assessed by confocal microscopy imaging.

2.13. SERS Measurements. Live SERS imaging was performed using a Raman microscope (inVia Reflex, Renishaw, U.K.) equipped with 1024 × 512 CDD detectors using a 785 nm laser excitation source and a 1200 L/mm diffraction grating. SERS maps were recorded using a 10× objective (numerical aperture, NA = 0.5) at 50% laser power (3.7 mW/μm^2 at the surface) and 1 s integration time. Samples were imaged in an Ibidi eight-well plate covered with a thin quartz slide. For SERS imaging, *xyz* maps of the selected volume were acquired with a resolution of 150 μm in *x* and *y* and 150 μm in *z*. For *z* slices, the map of one selected area was acquired with a resolution of 50 μm in *x* and 100 μm in *z*. SERS data were first analyzed using WiRE4.4 software (Renishaw, U.K.) to correct the baseline in the spectra and eliminate cosmic rays. Then, SERS mappings were analyzed by PCA in Matlab, which considers the full spectrum to assign the typical fingerprints of SERS tags.

https://doi.org/10.1021/acsami.4c04135
ACS Appl. Mater. Interfaces 2024, 16, 27151−27163

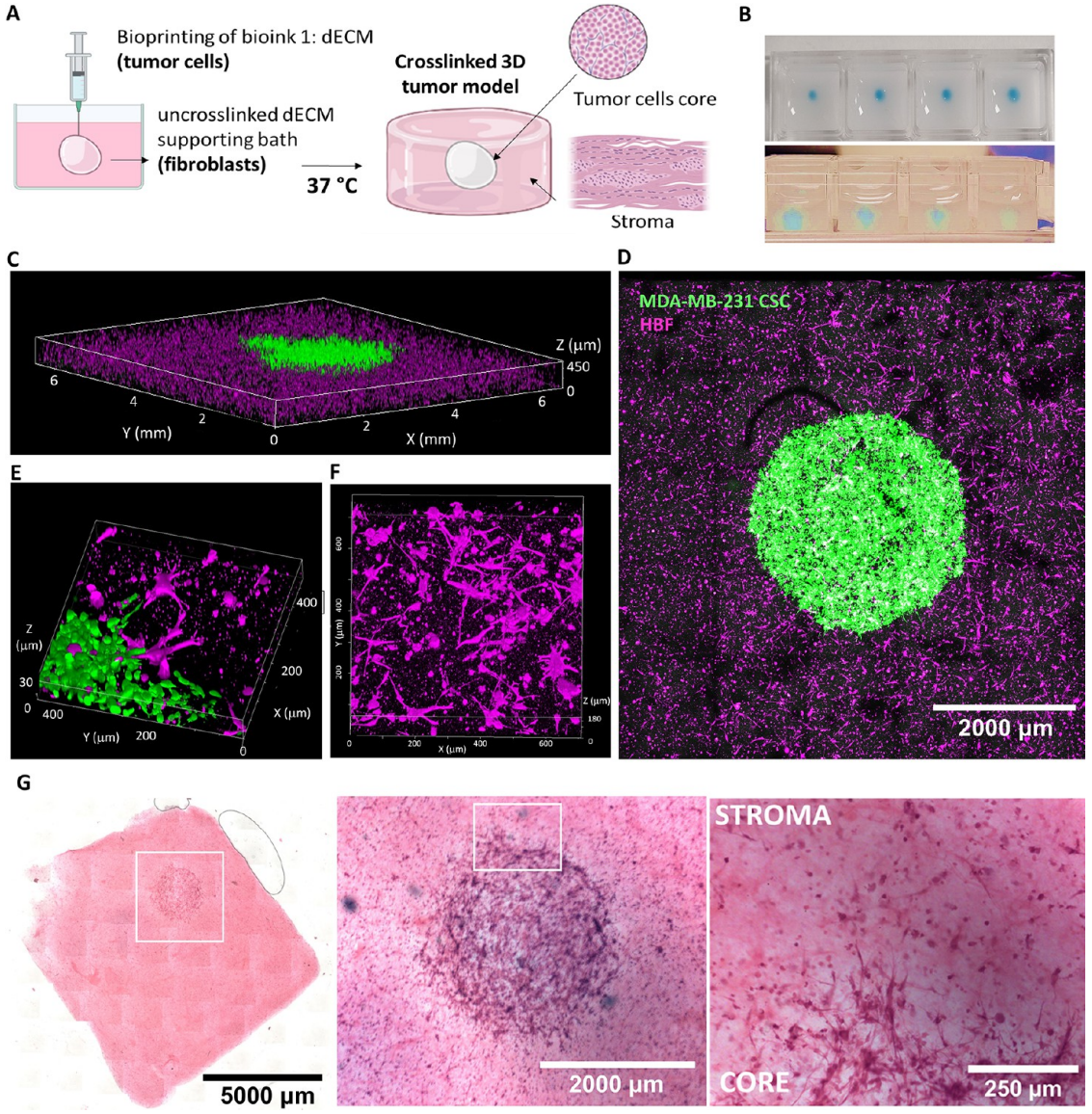

Figure 1. Development of bioprinted tumor-stroma models. (A) Schematic diagram illustrating the preparation of bioprinted tumor-stroma constructs. (B) Representative examples of cross-linked tumor-stroma models, showing upper and lateral views of the tumor core colored in blue, embedded in dECM. (C) Confocal 3D image reconstruction of a bioprinted 3D tumor-stroma model, depicting an inner core composed of CSCs (green) surrounded by HBFs (pink). (D) Live-cell confocal MIP fluorescence image of 3D CSC tumor-stroma model. (E) Confocal 3D image reconstruction depicting interactions between CSC and HBF compartments. (F) Confocal 3D image reconstruction showing HBF growing in the stromal compartment of the bioprinted tumor model. (G) Representative images of hematoxylin and eosin-stained 3D printed tumor-stroma tissue sections after 7 days in culture.

2.14. Drug Treatment and Therapeutic Response Studies. Doxorubicin, paclitaxel, docetaxel, and reparixin were purchased from Merck (original stocks: docetaxel 1.2 mM and reparixin 3.5 mM in dimethyl sulfoxide (DMSO), paclitaxel 1.17 mM in milli-Q water, and doxorubicin 1.8 mM in milli-Q water). CSC tumor-stroma models were bioprinted in a 96-well high-throughput testing plate (Ibidi). After 24 h, samples were exposed to increasing concentrations of docetaxel, paclitaxel, or doxorubicin in monoregimen or in combination with reparixin for 72 h. Control groups were nontreated cells cultured with a DMSO vehicle. Cell media was collected, and drug cytotoxicity was measured using the LDH assay (CyQUANT, Thermo), according to manufacturer instructions. Data shown in graphs represent a minimum of three biological replicates. LDH assay data were normalized to negative (control) and positive (Triton-X 100) cell death controls. Resulting dose−response curves were calculated using GraphPad Prism software through nonlinear regression analysis.

2.15. Statistical Analysis. Bar graphs and point graphs display mean value ± SEM. Statistical analysis consisted of normality data distribution assessment by the Kolmogorov−Smirnov test. Data fitting into a normal distribution was subjected to two-way analysis of variance (ANOVA) for multiple comparisons. Otherwise, non-parametric Bonferroni's test was employed for multiple mean comparisons. The significance threshold was established at $P < 0.05$ and significance levels were assigned *($0.01 \leq P < 0.05$), **($0.001 \leq P < 0.01$), ***($0.0001 \leq P$), **** ($0.00001 \leq P$). All analyses and graphs were performed using GraphPad Prism 6 software (GraphPad, San Diego, CA).

3. RESULTS AND DISCUSSION

3.1. Development of Bioprinted Triple-Negative-Breast CSC Tumor-Stroma Models. To mimic the complexity of the breast CSC-TME, we used bioprinting

https://doi.org/10.1021/acsami.4c04135
ACS Appl. Mater. Interfaces 2024, 16, 27151−27163

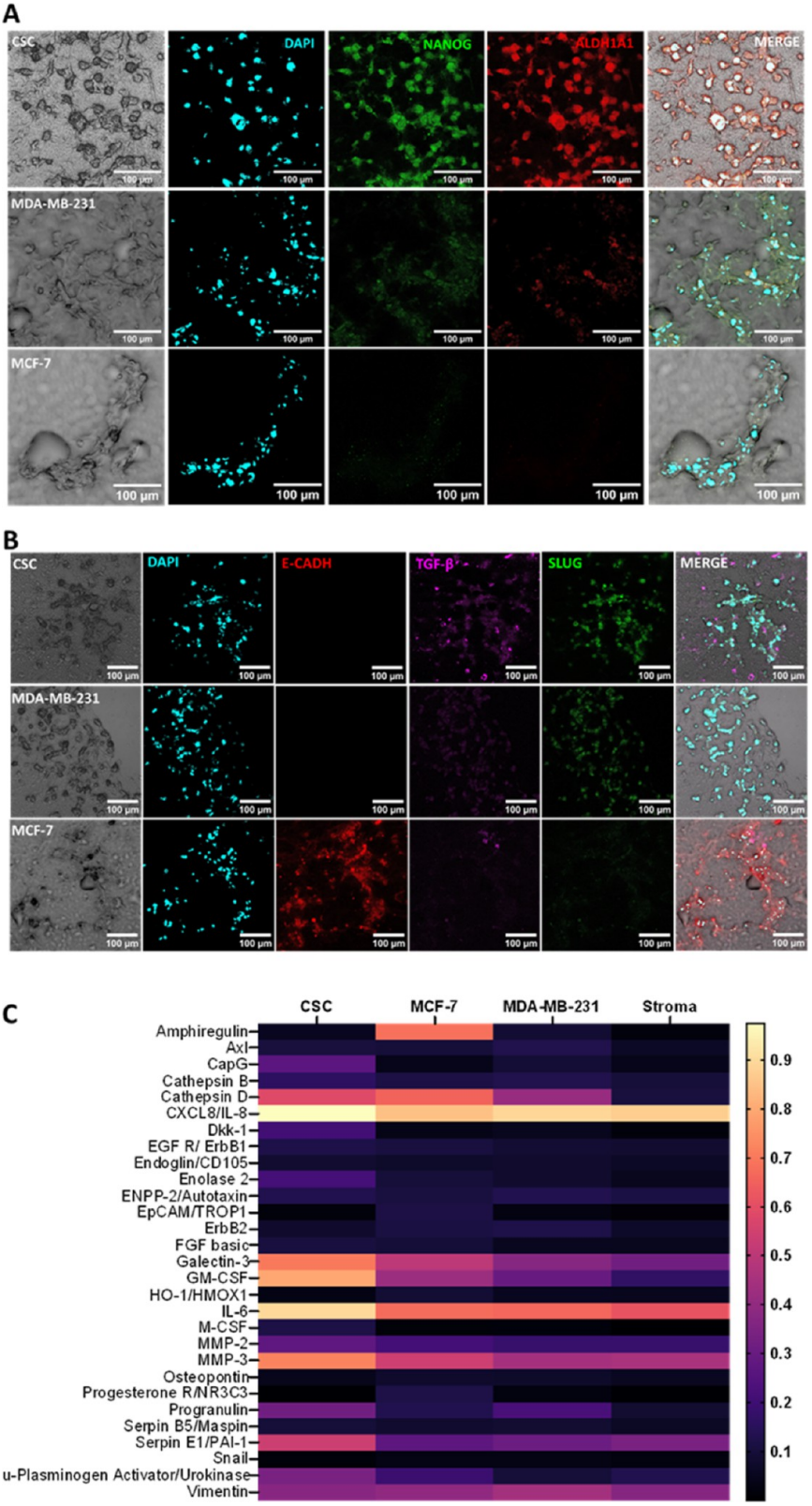

Figure 2. Biological characterization of breast tumor-stroma model subtypes. (A) Representative immunofluorescence (IF) images of the 3D tumor-stroma models, stained for NANOG (green) and ALDH1A1 (red) for the analysis of CSC biomarkers in the models and with DAPI (cyan) for cell nuclei. (B) Representative IF images of the 3D tumor-stroma models stained for E-cadherin (red), TGF-β (pink), and SLUG (green) for the analysis of epithelial-to-mesenchymal transition progression in tumor cells and with DAPI (cyan) for cell nuclei. (C) Heat-map indicating the oncoproteome in tumor-stroma and in stroma 3D models, measured using a microarray proteome profiler.

technology and porcine breast tissue-derived dECM to engineer a 3D TNBC−CSC tumor-stroma model. The dECM, previously characterized as a highly biocompatible bioink, supportive of cell growth[34] (Figure S1), retains original

https://doi.org/10.1021/acsami.4c04135
ACS Appl. Mater. Interfaces 2024, 16, 27151−27163

ECM-signaling molecules and ECM structural components such as collagen, making it a biologically relevant element for the model. To construct this model, we developed two different bioinks, namely, the tumor bioink and the stromal bioink. To generate the tumor bioink, CSCs isolated from the TNBC MDA-MB-231 cancer cell line were mixed with the dECM, whereas HBFs, which constitute the predominant stromal cell type in breast tumors, were embedded in the dECM to generate the stromal bioink. The detailed CSC isolation protocol is provided in the Experimental Section.

Inspired by the spatial arrangement typically observed in breast carcinomas,[15] the model design featured a central core composed of 100% tumor cells, encircled by stromal cells. Constructing this model was challenging because of the low viscosity of the dECM, a common issue in dECM bioprinting.[32] We therefore used the stromal bioink as a support bath for bioprinting the tumor core. To produce the 3D tumor-stroma model, the tumor bioink was printed by extrusion printing in the center of a 1 cm^2 well (Ibidi eight-well imaging slides) containing 300 μL of stromal bioink. The printing design consisted of a multilayered circle structure with a diameter of 1 mm. Detailed information on the tumor core bioprinting design and dimensions is provided in Figure S2A. The unique viscoelastic properties of the dECM allowed the printed core bioink to maintain its position and shape during extrusion, additionally enabling free motion of the printer nozzle through the stromal bioink. This procedure resulted in a structure where the core made of tumor cells was enveloped by the stromal compartment. The model was incubated at 37 °C to enable simultaneous cross-linking of both bioinks and render compartmentalized cell growth, thus producing a 3D tumor-stroma model (Figure 1A). Representative photographs of tumor-stroma replicates are displayed in Figure 1B, with additional bioprinting specifications detailed in the Experimental Section and in Figure S2.

Adjustable tumor core sizes, ranging from 0.7 to 3.2 mm in diameter, were achieved by varying the number of layers of the bioprinted cancer cell bioink, larger diameters being obtained by increasing the number of bioprinted layers and material deposition (Figures S2B,C and S3). For consistency, we standardized the number of bioprinted layers to 4, resulting in a tumor core of ca. 3 mm in diameter (Figure S3D). The bioprinted replicates consistently demonstrated similar size and shape, highlighting the effectiveness of this bioprinting technology to generate reproducible structures (Figure S3). Confocal imaging 3D reconstruction (Figure 1C) and MIP fluorescence images (Figures 1D and S3) provided insights into cell morphology and localization, as per the original bioprinting design. Magnifications and 3D reconstructions revealed distinct native cellular morphologies, including elongated filopodia in tumor cells and fibroblasts, indicating an optimal 3D ECM environment for each cell type, with fibroblasts displaying a morphology characteristic of breast tumor stroma (Figure 1E,F). Notably, the resulting images vividly illustrated active physical interconnections between HBF and CSC (Figures 1E and S4).

These interactions have been documented to be of crucial relevance in the evolution of breast tumors because fibroblasts are key mediators during tumor cell invasion, through cellular connections orchestrated by membrane cadherins.[45,46] Upon histological examination of the resulting 3D model, we confirmed the arrangement and morphology reminiscent of breast tumors, as depicted in Figures 1G and S5A.

We then extended our investigation to study immune cell behavior in bioprinted tumor-stroma models because immune cell infiltration plays a pivotal role in tumor evolution. THP-1 monocytes were thus incorporated, together with HBF, in the stromal compartment of the model. Confocal imaging was conducted to study monocyte dynamics over time (Figure S6A). As the culture progressed, monocyte proliferation and infiltration into the tumor compartment were observed (Figure S6B), establishing close contact with tumor cells. Notably, by day 10, certain monocytes underwent a discernible phenotypic transformation, exhibiting a significant increase in size (from 15 to 30 μm) and a variation in the morphology of their nuclei (Figure S6). Such changes have been reported to correspond to a differentiation of monocytes into macrophages.[47−49] Importantly, this transformation occurred naturally, i.e., no macrophage polarization inducers were added to the model. These observations suggest that signaling cues originating from the TME of the 3D model may play a crucial role in inducing monocyte polarization toward a tumor-associated macrophage (TAM) phenotype. This phenomenon has been previously described in 3D coculture models of tumor cells, fibroblasts, and monocytes.[50] From these data, we conclude that tumor-stroma models hold potential for future investigations aiming to unravel intricate interactions within the TME leading to activation of TAM populations.

3.2. Cancer Stem Cell Tumor-Stroma Models Exhibit a Distinct Molecular Signature. We next aimed to characterize the biological relevance of the CSC tumor-stroma model, when compared to other breast tumor-stroma model subtypes. Aiming to represent diverse breast tumor subtypes, we selected MDA-MB-231 and MCF-7 cells, representing heterogeneous TNBC and ER-positive tumor phenotypes, respectively, to form the core of the 3D model.

The models were cultured for 7 days and subsequently subjected to immunohistological analysis to examine the expression of CSC-associated markers among the different tumor subtypes. IF staining against NANOG and ALDH1A1 revealed a significantly higher expression of those markers in the CSC models, compared to other tumor-stroma model subtypes, which confirmed their enrichment in stem-like tumor cells (Figures 2A and S7). We next examined the expression of E-Cadherin, TGF-β, and SLUG proteins, which reflect different states of the epithelial-to-mesenchymal transition (EMT).[51,52] Immunofluorescence staining confirmed a significantly higher expression of SLUG and TGF-β biomarkers in cells, within the CSC tumor core, when compared to the other models. In contrast, MCF-7 tumor core cells displayed significantly higher levels of E-Cadherin, in agreement with their epithelial-like phenotype (Figures 2B and S7B). Data quantifying biomarker expression analyzed by IF staining is summarized in Figure S7B. Finally, we conducted a proteome profiler oncology array using cell lysates from four different samples: HBF alone (stroma), and MCF-7, MDA-MB-231, and CSC tumor-stroma models. Images of the membranes used for analysis are depicted in Figure S8. Membrane analysis revealed significant differences among the models (Figure 2C). Notably, the array unveiled the upregulation of several oncoprotein markers in the CSC model. Noteworthy among them was the expression of interleukin 8 (IL-8), galectin 3, granulocyte-macrophage colony-stimulating factor (GM-CSF), interleukin 6 (IL-6), matrix metalloproteinase-3 (MMP-3), and SERPIN E1. IL-8, prominently upregulated in the CSC model, plays a pivotal role in the breast TME by influencing

https://doi.org/10.1021/acsami.4c04135
ACS Appl. Mater. Interfaces 2024, 16, 27151−27163

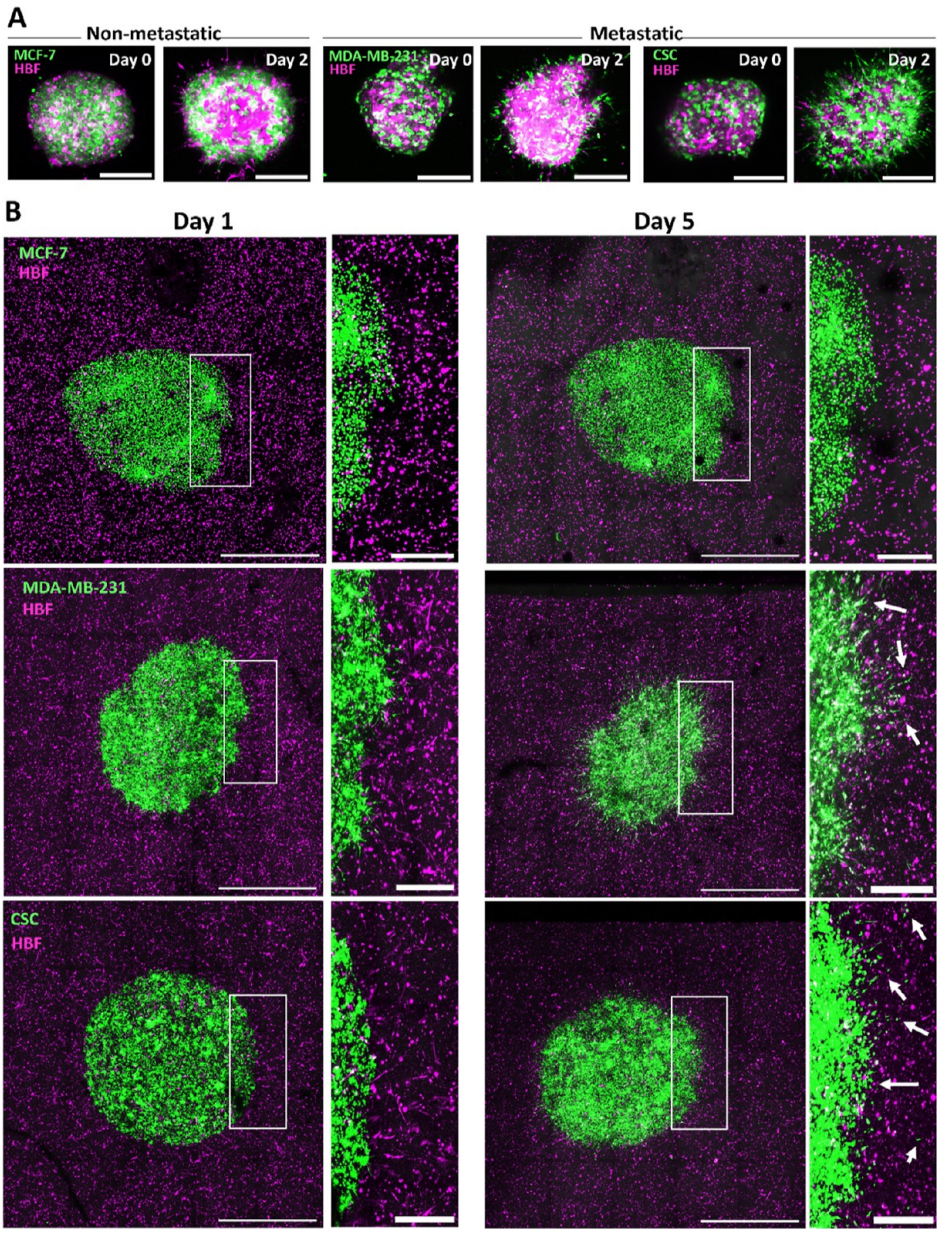

Figure 3. Evaluation of the metastatic potential of 3D-bioprinted tumor-stroma models. (A) MIP confocal images of MCF-7, MDA-MB-231, and CSC spheroids embedded in dECM at days 0 and 2 in culture. Scale bars: 200 μm. (B) MIP from z = 300 μm confocal images of MCF-7, MDA-MB-231, and CSC tumor-stroma models at days 1 and 5 in culture. White arrows indicate metastatic cells. Scale bars: 2000 μm (lower magnification) and 500 μm (higher magnification).

proinflammatory immune cell recruitment, promoting angiogenesis and tumor cell invasion, regulating CSC populations, and enhancing resistance to therapy.[53−55] Similarly, GM-CSF, which stimulates immune cell proliferation and activation, was upregulated in the 3D CSC tumor-stroma model, mirroring the inflammatory nature of the CSC TME.[56] Additionally, SERPIN E1, recognized as a crucial molecule in CSC formation,[57,58] was also upregulated in the model, along with MMP3—a key contributor of cancer progression and metastasis.[59,60] Last, a pronounced upregulation of IL-6 was detected in the CSC model, compared to the other conditions. It has been documented that IL-6 and IL-8 cytokines lead the transition of tumor cells toward CSC-like states.[61,62] Collectively, these findings underscore the ability of our model to faithfully reproduce the intrinsic molecular signature of CSC under 3D *in vitro* conditions.

3.3. CSC Tumor-Stroma Models Display Metastatic Potential through dECM. Metastatic potential is a critical factor influencing tumor progression and clinical outcomes in breast cancer patients.[63] Different tumor subtypes exhibit variations in metastatic potential, with HR-positive tumors of epithelial-like morphology typically demonstrating a lower metastatic potential, whereas TNBC tumors are commonly associated with a highly metastatic nature.[3,63] Moreover, metastasis is believed to be driven by selected CSC subpopulations.[64] We thus aimed to determine whether our CSC tumor-stroma models could reproduce the invasive behavior of TNBC tumors.

Traditionally, spheroid models have been regarded as the gold standard for the evaluation of invasive potential in 3D cultures.[65] Therefore, we aimed at an initial confirmation of the differences in invasive potential among all three cell lines, upon

https://doi.org/10.1021/acsami.4c04135
ACS Appl. Mater. Interfaces 2024, 16, 27151−27163

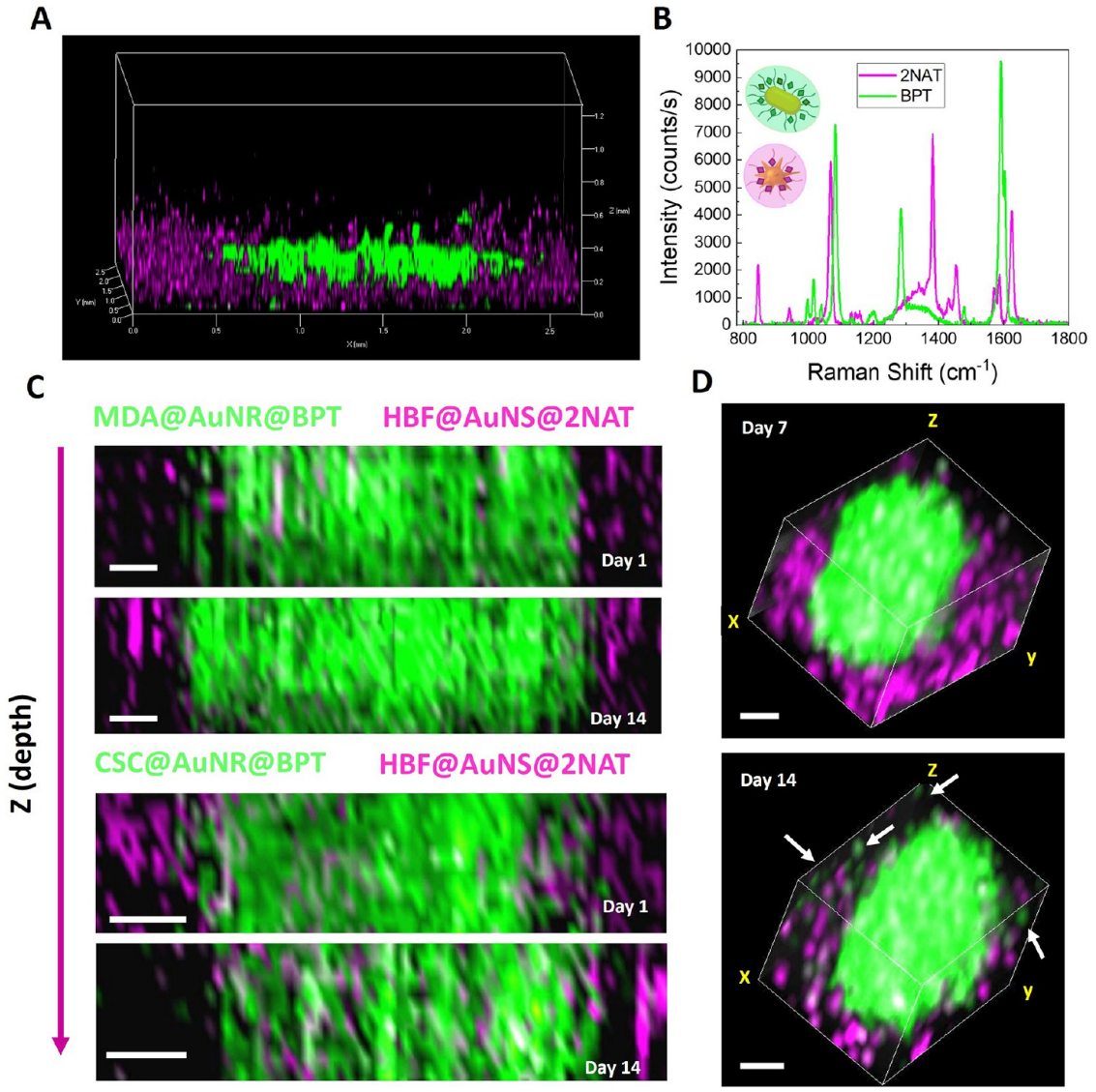

Figure 4. SERS imaging of 3D bioprinted tumor-stroma models. (A) MIP confocal image of CSC tumor-stroma models at day 7. (B) SERS spectra of AuNS@2NAT and AuNR@4BPT SERS tags used for cell labeling. (C) *z*-slices of the SERS signal of core and stromal cells after 1 and 14 days in culture. Scale bars: 500 μm. (D) 3D reconstruction of *xy* SERS maps taken every 150 μm in *z*. Dimensions: *xyz* = 1500 × 1700 × 1100 μm. White arrows indicate invasive CSCs. Scale bars: 500 μm.

integration of each cell line with HBF within a 3D spheroid model setup, to assess cancer cell invasion. After 48 h, both MDA-MB-231 and CSC were observed to exhibit pronounced invasion toward the dECM, in agreement with their expected higher invasive capacity, relative to the MCF-7 cell line. The results highlighted the exceptional migration capabilities of CSC toward the dECM, again emphasizing their aggressive phenotype (Figure 3A). These results align with previous findings regarding the exceptionally high invasive capacity of CSC in 2D invasion assays.[44]

We next aimed to reproduce these findings in our bioprinted tumor-stroma model framework. We thus bioprinted MCF-7, MDA-MB-231, and CSC tumor-stroma models, and then confocal imaging was conducted over time to monitor the behavior of cancer cells comprising the tumor cores. As anticipated, the MCF-7 tumor model displayed no migration toward the dECM, whereas both the MDA-MB-231 and CSC models exhibited distinct invasion toward the stromal compartment at day 5, compared to day 1 after bioprinting (Figure 3B). We can thus confirm that our 3D model successfully recreates the invasive potential of diverse tumor subtypes, providing a valuable platform for investigating tumor cell metastatic potential toward tumor stroma, in a configuration closely resembling breast carcinomas.

3.4. 3D SERS Imaging of Tumor-Stroma Model. When imaging our 3D model, we observed some limitations for in-depth imaging of the core due to its dimensions and excessive light scattering by the matrix (Figure 4A). Confocal imaging enabled us to track cell invasion from the tumor core toward the stromal compartment, but with limited z penetration, thereby missing important information regarding events occurring within the entire 3D model. As can be seen in Figure 4A, imaging of the model with CFM was only possible up to 600 μm and the entire core could not be imaged in 3D. Therefore, to complement the information provided by CFM, we employed SERS labeling of cells to study their dynamics over time. AuNSs functionalized with 2-naphthalenethiol (AuNS@2NAT) were used to label stromal cells, whereas

https://doi.org/10.1021/acsami.4c04135
ACS Appl. Mater. Interfaces 2024, 16, 27151−27163

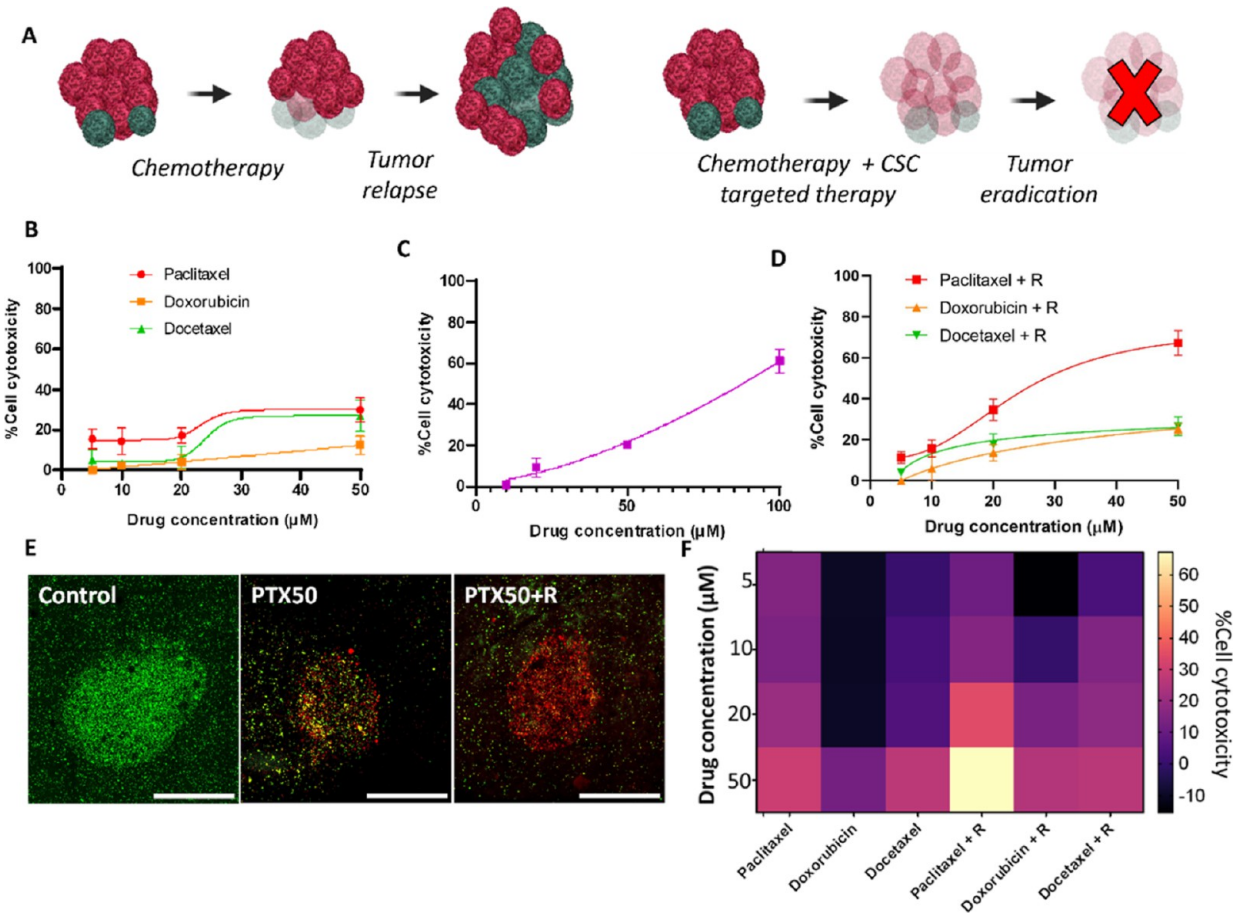

Figure 5. CSC-targeted therapy effectiveness in CSC tumor-stroma models. (A) Schematic illustration of the therapeutic strategy toward eliminating CSC populations. Red cells represent CSCs and green cells represent bulk tumor cells. Graphs depicting the drug dose−response curves in terms of cytotoxicity (%) in CSC 3D tumor-stroma models, exposed for 72 h to increasing concentrations of paclitaxel, doxorubicin, and docetaxel (b), reparixin (c) and paclitaxel, doxorubicin, and docetaxel in combination with reparixin (R) at 50 μM (D). Three biological replicates for each condition were analyzed, and mean ± SD is depicted in the graphs. Two-way ANOVA statistical analysis was performed. (E) Representative confocal fluorescence images of live/dead viability tests on CSC tumor-stroma models exposed to paclitaxel and to paclitaxel + reparixin (50 μM). Scale bars: 2 mm. (F) Summary heatmap indicating the percentage of cell cytotoxicity for each treatment at different drug concentrations.

AuNRs functionalized with 4-biphenylthiol (AuNR@4BPT) were employed for labeling tumor core invasive cells (MDA-MB-231 and CSC). Figure 4B shows the SERS spectra of both AuNR@4BPT and AuNS@2NAT SERS tags, revealing the characteristic fingerprint of each RaR. This combination of SERS tags was chosen to accurately distinguish the characteristic peaks at 1380 cm^{-1} for 2NAT and at 1280 cm^{-1} for 4BPT.

SERS maps in Figure 4C,D show a clear differentiation of both SERS tags from the core and the stroma, over the studied time points. To prevent cell death and ensure a meaningful SERS signal, the laser power employed for SERS excitation was carefully adjusted (3.7 mW μm^{-2}) to avoid excessive plasmonic heating. Indeed, SERS measurements were performed on the same model at different time points, with no visible signs of cell death associated with the measurements. First, z slices at the center of the model were obtained, taking SERS spectra every 50 μm in the x-plane and every 100 μm in the z-plane. SERS imaging allowed us to image the 3D core−shell model in z up to 1500 μm (Figure 4C). After 14 days *in vitro*, the SERS signal corresponding to AuNR@4BPT—located in the core of the model at initial time points—was also identified in the stroma (Figure 4D), suggesting CSC invasion into the stromal compartment. Therefore, the use of SERS imaging not only improved the z-depth imaging of the model, allowing cell tracking at deep z-planes, but also facilitated subsequent experimental analysis. Moreover, by avoiding the use of cell tracking fluorophores, multiplexing opportunities arise toward further fluorescence-based analysis, such as immunofluorescence labeling.

3.5. Evaluation of Targeted Therapies against Drug Resistance in Breast CSC. An essential aspect within breast cancer clinical treatment concerns the emergence of tumor chemoresistance post-therapy.[66] This phenomenon is associated with the proliferation of CSC clones, which demonstrate resistance to traditional chemotherapy, consequently contributing to tumor recurrence.[10] We first aimed to confirm that isolated CSC from the MDA-MB-231 cell line exhibits higher drug resistance, compared to their parental MDA-MB-231 counterparts, in a 2D culture setup. To this end, we conducted MTT assays to assess CSC and MDA-MB-231 cell viability, upon exposure to increasing concentrations of paclitaxel, a chemotherapy drug commonly used in the treatment of breast cancer. The results demonstrated significantly higher CSC viability at all tested concentrations, compared to the MDA-MB-231 parental cancer cells, supporting the notion of enhanced drug resistance mechanisms within the CSC

https://doi.org/10.1021/acsami.4c04135
ACS Appl. Mater. Interfaces 2024, 16, 27151−27163

population (Figure S9). Among the existing targeted therapies in clinical practice, reparixin emerges as a promising candidate, with an activity based on disrupting the crosstalk between IL-8 and its receptor CXCR1.[67−69] Proteome profiler analysis demonstrated that the 3D CSC model contains high levels of IL-8 interleukin, thus being a suitable platform for testing the use of this targeted therapy. Based on the premise that combination of conventional chemotherapy with CSC targeted therapy leads to tumor eradication, we devised a high-throughput drug test to optimize the regimen for eradicating CSC populations (Figure 5A). We therefore bioprinted CSC tumor-stroma models in a high-throughput 96-well plate (Figure S10). Following 3 days in culture, different therapeutic strategies were applied to the tumor-stroma models, including paclitaxel, docetaxel, and doxorubicin (all prominent chemotherapeutic compounds in breast cancer) at increasing concentrations (5, 10, 20, and 50 μM) either in monotherapy or in combination with 50 μM of reparixin. Concurrently, reparixin-targeted therapy was tested alone at concentrations of 10, 20, 50, and 100 μM. After 72 h of treatment, LDH cytotoxicity tests were performed to study drug efficacy. The results revealed that paclitaxel, docetaxel, and doxorubicin, in monotherapy regimens, display low cytotoxicity on the CSC-bioprinted tissue models (Figure 5B). Yet, reparixin-targeted monotherapy induced significant cytotoxicity at the highest concentrations (Figure 5C). Regarding the combination chemotherapy regimens, our results indicate that only paclitaxel in combination with reparixin achieved a significant cytotoxic effect in the model (mean ± SD = 67%), whereas no synergistic effect from reparixin was observed for docetaxel and doxorubicin treatments (Figure 5D). This cytotoxicity trend was additionally visualized using live/dead staining of the CSC model exposed to paclitaxel in monotherapy or in combination with reparixin. As shown in Figure 5E, higher propidium iodide (PI) staining was observed at the outer edge of the core in those models treated with paclitaxel, suggestive of a significant drug gradient, which may impede successful chemotherapeutic treatment of compact tumors. However, complete staining of the tumor core with PI was observed for the CSC model treated in a combination regimen, highlighting the effectiveness of this therapeutic approach. In contrast, live cells were found in the stromal compartment, suggesting that a significant fraction of fibroblasts remain alive after the treatment. While desired to avoid off-target cytotoxicity, this may be the reason for not achieving 100% cell cytotoxicity after treatments.

Collectively, these results enabled the development of a heatmap guiding the efficacy of each therapy combination, providing a visual indication of which combination therapy approach can be the most effective treatment against CSC populations (Figure 5F). Based on such a heatmap visualization, this type of preclinical drug testing might aid in selecting the preferred therapeutic regimen toward eradicating CSC in tumors that ultimately lead to relapse after conventional therapy.

In summary, our findings confirm the capability of developed CSC models to serve as drug-screening platforms for predicting the effectiveness of a given therapy against CSC populations. This approach holds promise for the efficient screening of numerous compounds in a condensed time frame, thereby expediting drug discovery in a more cost-effective manner.

4. CONCLUSIONS

The development of a bioprinted breast CSC tumor-stroma model, incorporating triple-negative breast CSCs (TNB-CSC) and stromal cells within a breast-derived dECM bioink, represents a significant advancement toward realistic 3D *in vitro* models. The comparison of molecular signatures with respect to other tumor-stroma models reveals a unique profile for artificial CSC tumor models. The model successfully recapitulates the invasive potential of TNB-CSC and overcomes imaging limitations through the use of SERS confocal microscopy. The high-throughput drug testing analysis conducted on this model demonstrates its efficacy as a promising drug-screening platform. The findings provide valuable insights into the efficacy of CSC-targeted therapy in combination with conventional chemotherapeutic compounds, particularly against CSC populations resistant to standard therapies. This approach holds promise toward accelerating drug discovery and improving therapeutic strategies for breast cancer.

■ ASSOCIATED CONTENT

Supporting Information

The Supporting Information is available free of charge at https://pubs.acs.org/doi/10.1021/acsami.4c04135.

Additional experimental details and materials, including photographs of experimental setup as well as characterization of the 3D model and drug experiments (PDF)

■ AUTHOR INFORMATION

Corresponding Author

Luis M. Liz-Marzán − *CIC biomaGUNE, Basque Research and Technology Alliance (BRTA), Donostia-San Sebastián 20014, Spain; Centro de Investigación Biomédica en Red, Bioingeniería, Biomateriales y Nanomedicina (CIBER-BBN), Barcelona 08035, Spain; Ikerbasque, Basque Foundation for Science, Bilbao 48009, Spain;* orcid.org/0000-0002-6647-1353; Email: llizmarzan@cicbiomagune.es

Authors

Patricia González-Callejo − *CIC biomaGUNE, Basque Research and Technology Alliance (BRTA), Donostia-San Sebastián 20014, Spain;* orcid.org/0000-0003-2963-4878

Clara García-Astrain − *CIC biomaGUNE, Basque Research and Technology Alliance (BRTA), Donostia-San Sebastián 20014, Spain; Centro de Investigación Biomédica en Red, Bioingeniería, Biomateriales y Nanomedicina (CIBER-BBN), Barcelona 08035, Spain;* orcid.org/0000-0002-4231-7335

Ada Herrero-Ruiz − *CIC biomaGUNE, Basque Research and Technology Alliance (BRTA), Donostia-San Sebastián 20014, Spain; Centro de Investigación Biomédica en Red, Bioingeniería, Biomateriales y Nanomedicina (CIBER-BBN), Barcelona 08035, Spain;* orcid.org/0009-0000-2071-2628

Malou Henriksen-Lacey − *CIC biomaGUNE, Basque Research and Technology Alliance (BRTA), Donostia-San Sebastián 20014, Spain; Centro de Investigación Biomédica en Red, Bioingeniería, Biomateriales y Nanomedicina (CIBER-BBN), Barcelona 08035, Spain;* orcid.org/0000-0003-3544-5846

Joaquín Seras-Franzoso − *Centro de Investigación Biomédica en Red, Bioingeniería, Biomateriales y Nanomedicina (CIBER-BBN), Barcelona 08035, Spain; Clinical Biochemistry, Drug Delivery and Therapy Group (CB-DDT), Vall d'Hebron Research Institute (VHIR), Vall d'Hebron University Hospital, Barcelona 08035, Spain; Department of Genetics and Microbiology, Universitat Autònoma de Barcelona (UAB), Bellaterra 08193, Spain;* orcid.org/0000-0002-7893-4773

Ibane Abasolo − *Centro de Investigación Biomédica en Red, Bioingeniería, Biomateriales y Nanomedicina (CIBER-BBN), Barcelona 08035, Spain; Clinical Biochemistry, Drug Delivery and Therapy Group (CB-DDT), Vall d'Hebron Research Institute (VHIR), Vall d'Hebron University Hospital, Barcelona 08035, Spain; Clinical Biochemistry Service, Vall d'Hebron University Hospital, Barcelona 08035, Spain*

Complete contact information is available at: https://pubs.acs.org/10.1021/acsami.4c04135

Author Contributions

The manuscript was written through contributions of all authors. All authors have given approval to the final version of the manuscript.

Notes

The authors declare the following competing financial interest(s): The authors declare that a patent application has been filed, which includes methods described in this manuscript.

■ ACKNOWLEDGMENTS

Funding Sources Financial support was provided by the European Research Council (ERC-AdG-2017 #787510 4DBIOSERS and ERC-2023-POC #101138255 3DTU-MOUR). C.G.A. thanks the Spanish State Research Agency for a Juan de la Cierva Incorporación Fellowship (FJCI-2016-28887). I.A. is grateful for the SGR grant from the Catalan Government (2021 SGR 1173). Figures were created using BioRender.

■ REFERENCES

(1) Sung, H.; Ferlay, J.; Siegel, R. L.; Laversanne, M.; Soerjomataram, I.; Jemal, A.; Bray, F. Global Cancer Statistics 2020: GLOBOCAN Estimates of Incidence and Mortality Worldwide for 36 Cancers in 185 Countries. *CA A Cancer J. Clin.* **2021**, *71*, 209−249.

(2) Shipitsin, M.; Campbell, L. L.; Argani, P.; Weremowicz, S.; Bloushtain-Qimron, N.; Yao, J.; Nikolskaya, T.; Serebryiskaya, T.; Beroukhim, R.; Hu, M.; Halushka, M. K.; Sukumar, S.; Parker, L. M.; Anderson, K. S.; Harris, L. N.; Garber, J. E.; Richardson, A. L.; Schnitt, S. J.; Nikolsky, Y.; Gelman, R. S.; Polyak, K. Molecular Definition of Breast Tumor Heterogeneity. *Cancer Cell* **2007**, *11*, 259−273.

(3) Van't Veer, L. J.; Dai, H.; Van de Vijver, M. J.; He, Y. D.; Hart, A. A. M.; Mao, M.; Peterse, H. L.; Van Der Kooy, K.; Marton, M. J.; Witteveen, A. T.; Schreiber, G. J.; Kerkhoven, R. M.; Roberts, C.; Linsley, P. S.; Bernards, R.; Friend, S. H. Gene Expression Profiling Predicts Clinical Outcome of Breast Cancer. *Nature* **2002**, *415*, 530−536.

(4) Dent, R.; Trudeau, M.; Pritchard, K. I.; Hanna, W. M.; Kahn, H. K.; Sawka, C. A.; Lickley, L. A.; Rawlinson, E.; Sun, P.; Narod, S. A. Triple-Negative Breast Cancer: Clinical Features and Patterns of Recurrence. *Clin. Cancer Res.* **2007**, *13*, 4429−4434.

(5) Kim, C.; Gao, R.; Sei, E.; Brandt, R.; Hartman, J.; Hatschek, T.; Crosetto, N.; Foukakis, T.; Navin, N. E. Chemoresistance Evolution in Triple-Negative Breast Cancer Delineated by Single-Cell Sequencing. *Cell* **2018**, *173*, 879−893.e13.

(6) Zheng, Q.; Zhang, M.; Zhou, F.; Zhang, L.; Meng, X. The Breast Cancer Stem Cells Traits and Drug Resistance. *Front. Pharmacol* **2021**, *11*, 599965.

(7) Hua, Z.; White, J.; Zhou, J. Cancer Stem Cells in TNBC. *Semin. Cancer Biol.* **2022**, *82*, 26−34.

(8) Butti, R.; Gunasekaran, V. P.; Kumar, T. V. S.; Banerjee, P.; Kundu, G. C. Breast Cancer Stem Cells: Biology and Therapeutic Implications. *Int. J. Biochem. Cell Biol.* **2019**, *107*, 38−52.

(9) Liu, H.; Patel, M. R.; Prescher, J. A.; Patsialou, A.; Qian, D.; Lin, J.; Wen, S.; Chang, Y. F.; Bachmann, M. H.; Shimono, Y.; Dalerba, P.; Adorno, M.; Lobo, N.; Bueno, J.; Dirbas, F. M.; Goswami, S.; Somlo, G.; Condeelis, J.; Contag, C. H.; Gambhir, S. S.; Clarke, M. F. Cancer Stem Cells from Human Breast Tumors Are Involved in Spontaneous Metastases in Orthotopic Mouse Models. *Proc. Natl. Acad. Sci. U.S.A.* **2010**, *107*, 18115−18120.

(10) Morrison, B. J.; Schmidt, C. W.; Lakhani, S. R.; Reynolds, B. A.; Lopez, J. A. Breast Cancer Stem Cells: Implications for Therapy of Breast Cancer. *Breast Cancer Res.* **2008**, *10*, 210.

(11) Saygin, C.; Matei, D.; Majeti, R.; Reizes, O.; Lathia, J. D. Targeting Cancer Stemness in the Clinic: From Hype to Hope. *Cell Stem Cell* **2019**, *24*, 25−40.

(12) Lehmann, B. D.; Bauer, J. A.; Chen, X.; Sanders, M. E.; Chakravarthy, A. B.; Shyr, Y.; Pietenpol, J. A. Identification of Human Triple-Negative Breast Cancer Subtypes and Preclinical Models for Selection of Targeted Therapies. *J. Clin. Invest.* **2011**, *121*, 2750−2767.

(13) Landeros, N.; Castillo, I.; Pérez-Castro, R. Preclinical and Clinical Trials of New Treatment Strategies Targeting Cancer Stem Cells in Subtypes of Breast Cancer. *Cells* **2023**, *12*, 720.

(14) Jensen, C.; Teng, Y. Is It Time to Start Transitioning From 2D to 3D Cell Culture? *Front. Mol. Biosci.* **2020**, *7*, 33.

(15) Structure of the Tumor Stroma Predicts Invasive Breast Cancer Relapse. *Cancer Discov.* **2022**, *12*, 597. 1158/2159−8290.CD-RW2022−014.

(16) Anderson, N. M.; Simon, M. C. The Tumor Microenvironment. *Curr. Biol.* **2020**, *30*, 921−925.

(17) Swartz, M. A.; Iida, N.; Roberts, E. W.; Sangaletti, S.; Wong, M. H.; Yull, F. E.; Coussens, L. M.; DeClerck, Y. A. Tumor Microenvironment Complexity: Emerging Roles in Cancer Therapy. *Cancer Res.* **2012**, *72*, 2473−2480.

(18) Allinen, M.; Beroukhim, R.; Cai, L.; Brennan, C.; Lahti-Domenici, J.; Huang, H.; Porter, D.; Hu, M.; Chin, L.; Richardson, A.; Schnitt, S.; Sellers, W. R.; Polyak, K. Molecular Characterization of the Tumor Microenvironment in Breast Cancer. *Cancer Cell* **2004**, *6*, 17−32.

(19) Li, W.; Zhou, Z.; Zhou, X.; Khoo, B. L.; Gunawan, R.; Chin, Y. R.; Zhang, L.; Yi, C.; Guan, X.; Yang, M. 3D Biomimetic Models to Reconstitute Tumor Microenvironment In Vitro: Spheroids, Organoids, and Tumor-on-a-Chip. *Adv. Healthcare Mater.* **2023**, *12*, 2202609.

(20) Datta, P.; Dey, M.; Ataie, Z.; Unutmaz, D.; Ozbolat, I. T. 3D Bioprinting for Reconstituting the Cancer Microenvironment. *npj Precis. Oncol.* **2020**, *4*, 18.

(21) Zhang, Y. S.; Duchamp, M.; Oklu, R.; Ellisen, L. W.; Langer, R.; Khademhosseini, A. Bioprinting the Cancer Microenvironment. *ACS Biomater. Sci. Eng.* **2016**, *2*, 1710−1721.

(22) Leberfinger, A. N.; Dinda, S.; Wu, Y.; Koduru, S. V.; Ozbolat, V.; Ravnic, D. J.; Ozbolat, I. T. Bioprinting Functional Tissues. *Acta Biomater.* **2019**, *95*, 32−49.

(23) Germain, N.; Dhayer, M.; Dekiouk, S.; Marchetti, P. Current Advances in 3D Bioprinting for Cancer Modeling and Personalized Medicine. *Int. J. Mol. Sci.* **2022**, *23*, 3432.

(24) Murphy, S. V.; Atala, A. 3D Bioprinting of Tissues and Organs. *Nat. Biotechnol.* **2014**, *32*, 773−785.

(25) Wang, Y.; Shi, W.; Kuss, M.; Mirza, S.; Qi, D.; Krasnoslobodtsev, A.; Zeng, J.; Band, H.; Band, V.; Duan, B. 3D

Bioprinting of Breast Cancer Models for Drug Resistance Study. *ACS Biomater. Sci. Eng.* **2018**, *4*, 4401−4411.
(26) Augustine, R.; Kalva, S. N.; Ahmad, R.; Zahid, A. A.; Hasan, S.; Nayeem, A.; McClements, L.; Hasan, A. 3D Bioprinted Cancer Models: Revolutionizing Personalized Cancer Therapy. *Transl. Oncol.* **2021**, *14*, 101015.
(27) Khoeini, R.; Nosrati, H.; Akbarzadeh, A.; Eftekhari, A.; Kavetskyy, T.; Khalilov, R.; Ahmadian, E.; Nasibova, A.; Datta, P.; Roshangar, L.; Deluca, D. C.; Davaran, S.; Cucchiarini, M.; Ozbolat, I. T. Natural and Synthetic Bioinks for 3D Bioprinting. *Adv. NanoBiomed Res.* **2021**, *1*, 2000097.
(28) Morgan, F. L. C.; Moroni, L.; Baker, M. B. Dynamic Bioinks to Advance Bioprinting. *Adv. Healthcare Mater.* **2020**, *9* (15), 1901798.
(29) Gu, Y.; Forget, A.; Shastri, V. P. Biobridge: An Outlook on Translational Bioinks for 3D Bioprinting. *Adv. Sci.* **2022**, *9*, 2103469.
(30) De Santis, M. M.; Alsafadi, H. N.; Tas, S.; Bölükbas, D. A.; Prithiviraj, S.; Da Silva, I. A. N.; Mittendorfer, M.; Ota, C.; Stegmayr, J.; Daoud, F.; Königshoff, M.; Swärd, K.; Wood, J. A.; Tassieri, M.; Bourgine, P. E.; Lindstedt, S.; Mohlin, S.; Wagner, D. E. Extracellular-Matrix-Reinforced Bioinks for 3D Bioprinting Human Tissue. *Adv. Mater.* **2021**, *33*, 2005476.
(31) Abaci, A.; Guvendiren, M. Designing Decellularized Extracellular Matrix-Based Bioinks for 3D Bioprinting. *Adv. Healthcare Mater.* **2020**, *9*, 2000734.
(32) Zhang, H.; Wang, Y.; Zheng, Z.; Wei, X.; Chen, L.; Wu, Y.; Huang, W.; Yang, L. Strategies for Improving the 3D Printability of Decellularized Extracellular Matrix Bioink. *Theranostics* **2023**, *13*, 2562−2587.
(33) Xu, J.; Yang, S.; Su, Y.; Hu, X.; Xi, Y.; Cheng, Y. Y.; Kang, Y.; Nie, Y.; Pan, B.; Song, K. A 3D Bioprinted Tumor Model Fabricated with Gelatin/Sodium Alginate/Decellularized Extracellular Matrix Bioink. *Int. J. Bioprint.* **2022**, *9*, 630.
(34) González-Callejo, P.; Vázquez-Aristizabal, P.; García-Astrain, C.; Jimenez de Aberasturi, D.; Henriksen-Lacey, M.; Izeta, A.; Liz-Marzán, L. M. 3D Bioprinted Breast Tumor-Stroma Models for Pre-Clinical Drug Testing. *Mater. Today Bio* **2023**, *23*, 100826.
(35) Jimenez de Aberasturi, D.; Henriksen-Lacey, M.; Litti, L.; Langer, J.; Liz-Marzán, L. M. Using SERS Tags to Image the Three-Dimensional Structure of Complex Cell Models. *Adv. Funct. Mater.* **2020**, *30*, 1909655.
(36) Lenzi, E.; Jimenez De Aberasturi, D.; Henriksen-Lacey, M.; Piñeiro, P.; Muniz, A. J.; Lahann, J.; Liz-Marzán, L. M. SERS and Fluorescence-Active Multimodal Tessellated Scaffolds for Three-Dimensional Bioimaging. *ACS Appl. Mater. Interfaces* **2022**, *14*, 20708−20719.
(37) Castellanos-Rubio, I.; Rodrigo, I.; Olazagoitia-Garmendia, A.; Arriortua, O.; Gil De Muro, I.; Garitaonandia, J. S.; Bilbao, J. R.; Fdez-Gubieda, M. L.; Plazaola, F.; Orue, I.; Castellanos-Rubio, A.; Insausti, M. Highly Reproducible Hyperthermia Response in Water, Agar, and Cellular Environment by Discretely PEGylated Magnetite Nanoparticles. *ACS Appl. Mater. Interfaces* **2020**, *12*, 27917−27929.
(38) Huang, W.; Wu, X.; Zhao, Y.; Liu, Y.; Zhang, B.; Qiao, M.; Zhu, Z.; Zhao, Z. Janus-Inspired Core-Shell Structure Hydrogel Programmatically Releases Melatonin for Reconstruction of Post-operative Bone Tumor. *ACS Appl. Mater. Interfaces* **2023**, *15*, 2639−2655.
(39) Herrero-Ruiz, A.; Carolo, G.; González-Rubio, G.; Grzelczak, M.; Niehaus, J. S.; Weller, H.; Liz-Marzán, L. M. Millifluidic Flow Reactor for Reproducible Seed-Mediated Nanoparticle Synthesis. *J. Phys. Chem. C* **2023**, *127*, 19747−19758.
(40) Jimenez De Aberasturi, D.; Serrano-Montes, A. B.; Langer, J.; Henriksen-Lacey, M.; Parak, W. J.; Liz-Marzán, L. M. Surface Enhanced Raman Scattering Encoded Gold Nanostars for Multiplexed Cell Discrimination. *Chem. Mater.* **2016**, *28*, 6779−6790.
(41) Gener, P.; Gouveia, L. P.; Sabat, G. R.; de Sousa Rafael, D. F.; Fort, N. B.; Arranja, A.; Fernández, Y.; Prieto, R. M.; Ortega, J. S.; Arango, D.; Abasolo, I.; Videira, M.; Schwartz, S. Fluorescent CSC Models Evidence That Targeted Nanomedicines Improve Treatment Sensitivity of Breast and Colon Cancer Stem Cells. *Nanomedicine* **2015**, *11*, 1883−1892.
(42) Cámara-Sánchez, P.; Díaz-Riascos, Z. V.; García-Aranda, N.; Gener, P.; Seras-Franzoso, J.; Giani-Alonso, M.; Royo, M.; Vázquez, E.; Schwartz, S.; Abasolo, I. Selectively Targeting Breast Cancer Stem Cells by 8-Quinolinol and Niclosamide. *Int. J. Mol. Sci.* **2022**, *23*, 11760.
(43) Gener, P.; Rafael, D.; Seras-franzoso, J.; Perez, A.; Pindado, L. A.; Casas, G.; Arango, D.; Fernández, Y.; Díaz-riascos, Z. V.; Abasolo, I.; Schwartz, S. Pivotal Role of AKT2 during Dynamic Phenotypic Change of Breast Cancer Stem Cells. *Cancers* **2019**, *11*, 1058.
(44) González-Callejo, P.; Gener, P.; Díaz-Riascos, Z. V.; Conti, S.; Cámara-Sánchez, P.; Riera, R.; Mancilla, S.; García-Gabilondo, M.; Peg, V.; Arango, D.; Rosell, A.; Labernadie, A.; Trepat, X.; Albertazzi, L.; Schwartz, S.; Seras-Franzoso, J.; Abasolo, I. Extracellular Vesicles Secreted by Triple-Negative Breast Cancer Stem Cells Trigger Premetastatic Niche Remodeling and Metastatic Growth in the Lungs. *Int. J. Cancer* **2023**, *152*, 2153−2165.
(45) Hu, D.; Li, Z.; Zheng, B.; Lin, X.; Pan, Y.; Gong, P.; Zhuo, W.; Hu, Y.; Chen, C.; Chen, L.; Zhou, J.; Wang, L. Cancer-Associated Fibroblasts in Breast Cancer: Challenges and Opportunities. *Cancer Commun.* **2022**, *42*, 401−434.
(46) Yu, Y.; Xiao, C. H.; Tan, L. D.; Wang, Q. S.; Li, X. Q.; Feng, Y. M. Cancer-associated fibroblasts induce epithelial−mesenchymal transition of breast cancer cells through paracrine TGF-β signalling. *Br. J. Cancer* **2014**, *110*, 724−732.
(47) Dannhauser, D.; Rossi, D.; De Gregorio, V.; Netti, P. A.; Terrazzano, G.; Causa, F. Single Cell Classification of Macrophage Subtypes by Label-Free Cell Signatures and Machine Learning. *R. Soc. Open Sci.* **2022**, *9* (9), 220270.
(48) Sapudom, J.; Karaman, S.; Mohamed, W. K. E.; Garcia-Sabaté, A.; Quartey, B. C.; Teo, J. C. M. 3D in Vitro M2Macrophage Model to Mimic Modulation of Tissue Repair. *npj Regener. Med.* **2021**, *6*, 83.
(49) Sridharan, R.; Cameron, A. R.; Kelly, D. J.; Kearney, C. J.; O'Brien, F. J. Biomaterial Based Modulation of Macrophage Polarization: A Review and Suggested Design Principles. *Mater. Today* **2015**, *18*, 313−325.
(50) Rebelo, S. P.; Pinto, C.; Martins, T. R.; Harrer, N.; Estrada, M. F.; Loza-Alvarez, P.; Cabeçadas, J.; Alves, P. M.; Gualda, E. J.; Sommergruber, W.; Brito, C. 3D-3-Culture: A Tool to Unveil Macrophage Plasticity in the Tumour Microenvironment. *Biomaterials* **2018**, *163*, 185−197.
(51) Tanabe, S.; Quader, S.; Cabral, H.; Ono, R. Interplay of EMT and CSC in Cancer and the Potential Therapeutic Strategies. *Front. Pharmacol* **2020**, *11*, 904.
(52) Shibue, T.; Weinberg, R. A. EMT, CSCs, and Drug Resistance: The Mechanistic Link and Clinical Implications. *Nat. Rev. Clin. Oncol.* **2017**, *14*, 611−629.
(53) Singh, J. K.; Simões, B. M.; Howell, S. J.; Farnie, G.; Clarke, R. B. Recent Advances Reveal IL-8 Signaling as a Potential Key to Targeting Breast Cancer Stem Cells. *Breast Cancer Res.* **2013**, *15*, 210.
(54) Ginestier, C.; Liu, S.; Diebel, M. E.; Korkaya, H.; Luo, M.; Brown, M.; Wicinski, J.; Cabaud, O.; Charafe-Jauffret, E.; Birnbaum, D.; Guan, J. L.; Dontu, G.; Wicha, M. S. CXCR1 Blockade Selectively Targets Human Breast Cancer Stem Cells in Vitro and in Xenografts. *J. Clin. Invest.* **2010**, *120*, 485−497.
(55) Ma, Y.; Ren, Y.; Dai, Z. J.; Wu, C. J.; Ji, Y. H.; Xu, J. IL-6, IL-8 and TNF-α Levels Correlate with Disease Stage in Breast Cancer Patients. *Adv. Clin. Exp. Med.* **2017**, *26*, 421−426.
(56) Su, X.; Xu, Y.; Fox, G. C.; Xiang, J.; Kwakwa, K. A.; Davis, J. L.; Belle, J. I.; Lee, W. C.; Wong, W. H.; Fontana, F.; Hernandez-Aya, L. F.; Kobayashi, T.; Tomasson, H. M.; Su, J.; Bakewell, S. J.; Stewart, S. A.; Egbulefu, C.; Karmakar, P.; Meyer, M. A.; Veis, D. J.; DeNardo, D. G.; Lanza, G. M.; Achilefu, S.; Weilbaecher, K. N. Breast Cancer-Derived GM-CSF Regulates Arginase 1 in Myeloid Cells to Promote an Immunosuppressive Microenvironment. *J. Clin. Invest.* **2021**, *131*, No. e145296.

https://doi.org/10.1021/acsami.4c04135
ACS Appl. Mater. Interfaces 2024, 16, 27151−27163

(57) Zhang, Q.; Lei, L.; Jing, D. Knockdown of SERPINE1 Reverses Resistance of Triple-Negative Breast Cancer to Paclitaxel via Suppression of VEGFA. *Oncol. Rep.* **2020**, *44*, 1875−1884.
(58) Su, Y. H.; Wu, Y. Z.; Ann, D. K.; Chen, J. L. Y.; Kuo, C. Y. Obesity Promotes Radioresistance through SERPINE1-Mediated Aggressiveness and DNA Repair of Triple-Negative Breast Cancer. *Cell Death Dis.* **2023**, *14*, 53.
(59) Chu, C.; Liu, X.; Bai, X.; Zhao, T.; Wang, M.; Xu, R.; Li, M.; Hu, Y.; Li, W.; Yang, L.; Qin, Y.; Yang, M.; Yan, C.; Zhang, Y. MiR-519d Suppresses Breast Cancer Tumorigenesis and Metastasis via Targeting MMP3. *Int. J. Biol. Sci.* **2018**, *14*, 228−236.
(60) Suhaimi, S. A.; Chan, S. C.; Rosli, R. Matrix Metallopeptidase 3 Polymorphisms: Emerging Genetic Markers in Human Breast Cancer Metastasis. *J. Breast Cancer* **2020**, *23* (1), 1−9.
(61) Chen, W.; Qin, Y.; Liu, S. Cytokines, Breast Cancer Stem Cells (BCSCs) and Chemoresistance. *Clin. Transl. Med.* **2018**, *7*, No. e27.
(62) Korkaya, H.; Liu, S.; Wicha, M. S. Breast Cancer Stem Cells, Cytokine Networks, and the Tumor Microenvironment. *J. Clin. Invest.* **2011**, *121*, 3804−3809.
(63) Riggio, A. I.; Varley, K. E.; Welm, A. L. The Lingering Mysteries of Metastatic Recurrence in Breast Cancer. *Br. J. Cancer* **2021**, *124*, 13−26.
(64) Peitzsch, C.; Tyutyunnykova, A.; Pantel, K.; Dubrovska, A. Cancer Stem Cells: The Root of Tumor Recurrence and Metastases. *Semin. Cancer Biol.* **2017**, *44*, 10−24.
(65) Fennema, E.; Rivron, N.; Rouwkema, J.; van Blitterswijk, C.; De Boer, J. Spheroid Culture as a Tool for Creating 3D Complex Tissues. *Trends Biotechnol.* **2013**, *31*, 108−115.
(66) Koren, S.; Bentires-Alj, M. Breast Tumor Heterogeneity: Source of Fitness, Hurdle for Therapy. *Mol. Cell* **2015**, *60*, 537−546.
(67) Schott, A. F.; Goldstein, L. J.; Cristofanilli, M.; Ruffini, P. A.; McCanna, S.; Reuben, J. M.; Perez, R. P.; Kato, G.; Wicha, M. Phase Ib Pilot Study to Evaluate Reparixin in Combination with Weekly Paclitaxel in Patients with HER-2-Negative Metastatic Breast Cancer. *Clin. Cancer Res.* **2017**, *23*, 5358−5365.
(68) Brandolini, L.; Cristiano, L.; Fidoamore, A.; De Pizzol, M.; Di Giacomo, E.; Florio, T. M.; Confalone, G.; Galante, A.; Cinque, B.; Benedetti, E.; Ruffini, P. A.; Cifone, M. G.; Giordano, A.; Alecci, M.; Allegretti, M.; Cimini, A. Targeting CXCR1 on Breast Cancer Stem Cells: Signaling Pathways and Clinical Application Modelling. *Oncotarget* **2015**, *6*, 43375−43394.
(69) Ruffini, P. A. The CXCL8-CXCR1/2 Axis as a Therapeutic Target in Breast Cancer Stem-like Cells. *Front. Oncol.* **2019**, *9*, 40.

https://doi.org/10.1021/acsami.4c04135
ACS Appl. Mater. Interfaces 2024, 16, 27151−27163